Developing a Fundamental Knowledge Base for the Interaction of Ruthenium with Natural and Engineered Iron-Bearing Materials

September 2021

Eugene S. Ilton (PI)
Neil Henson
Michel Sassi
Josef Matyas

DISCLAIMER

This report was prepared as an account of work sponsored by an agency of the United States Government. Neither the United States Government nor any agency thereof, nor Battelle Memorial Institute, nor any of their employees, **makes any warranty, express or implied, or assumes any legal liability or responsibility for the accuracy, completeness, or usefulness of any information, apparatus, product, or process disclosed, or represents that its use would not infringe privately owned rights**. Reference herein to any specific commercial product, process, or service by trade name, trademark, manufacturer, or otherwise does not necessarily constitute or imply its endorsement, recommendation, or favoring by the United States Government or any agency thereof, or Battelle Memorial Institute. The views and opinions of authors expressed herein do not necessarily state or reflect those of the United States Government or any agency thereof.

PACIFIC NORTHWEST NATIONAL LABORATORY
operated by
BATTELLE
for the
UNITED STATES DEPARTMENT OF ENERGY
under Contract DE-AC05-76RL01830

Printed in the United States of America

Available to DOE and DOE contractors from
the Office of Scientific and Technical Information,
P.O. Box 62, Oak Ridge, TN 37831-0062
www.osti.gov
ph: (865) 576-8401
fox: (865) 576-5728
email: reports@osti.gov

Available to the public from the National Technical Information Service
5301 Shawnee Rd., Alexandria, VA 22312
ph: (800) 553-NTIS (6847)
or (703) 605-6000
email: info@ntis.gov
Online ordering: http://www.ntis.gov

Developing a Fundamental Knowledge Base for the Interaction of Ruthenium with Natural and Engineered Iron-Bearing Materials

September 2021

Eugene S. Ilton (PI)
Neil Henson
Michel Sassi
Josef Matyas

Pacific Northwest National Laboratory
Richland, Washington 99354

1.0   Introduction

The intent of this project is to build a fundamental knowledge base concerning the redox coupling between Ru and Fe in heterogeneous systems with predictive applications towards the fate, speciation, and transport of Ru in the environment and its capture using available technologies. The former addresses the utility of Ru as a forensic tool to trace, for example, the origin and severity of nuclear accidents as well as assessing the threat of radiotoxic Ru to the public health. The focus on Fe stems from its ubiquity in the near-surface of the Earth, the primary control it exerts over electron cycling in environmental systems, and its prevalence in engineered materials whether part of the infrastructure of a nuclear power/reprocessing plant, the primary component of steel canisters used for storage of nuclear waste, or the sorbent material used to effectively capture Ru. The objectives neatly bookend very different forms of Ru and Fe that can occur in the environment and reprocessing facilities, and contrasts the coupled reduction of Fe(III) and oxidation of Ru(III, II) versus the coupled oxidation of Fe(II) and reduction of Ru(IV-VIII).

Objective 1. Determine at a fundamental predictive level why $Ru^{3+, 2+}$ adsorbs irreversibly under environmentally relevant conditions to Fe oxides.[1] We will focus on ferrihydrite (fh), nominally $Fe(OH)_3$, a common precursor to more stable Fe(oxy)(hydr)oxides and hematite, Fe_2O_3. We note that the effective ionic radii of Ru(III) and Ru(IV) are close to Fe(II) and Fe(III) respectively. Importantly, it is often the case that the surface of steel/iron bearing structures have a variably thick corrosion layer. Consequently, this task also has relevance to the interaction of Ru ions with infrastructure materials (see review by Mun et al.[3]).

Objective 2. Determine the coordination environment of Ru associated with hematite that formed by annealing Ru-fh synthesized in Objective 1 at elevated temperatures. This is relevant to ascertaining the stability of Ru-Fe oxides associations during pyrogenic events as well as better understanding why doping hematite with Ru enhances the photocatalytic properties of hematite.

Objective 3.   Determine the redox reactivity of $Fe^{3+}(aq)$ and $RuNOCl_3$ in the homogeneous aqueous phase.

Objective 4. In contrast, starting with Fe in the aqueous phase and Ru in the solid phase ($RuO_2 \cdot nH_2O$), determine the ability of $Fe^{2+}(aq)$ to reduce $RuO_2 \cdot nH_2O(s)$ to lower valent more soluble species as function of pH and Fe^{2+} activity.   Our working _hypothesis_ is that release of Ru to the environment, in the absence of strongly complexing ligands, will depend on exceeding the coupled proton-electron storage capacity of RuO_2 which is a well-known supercapacitor. However, complications (of interest) might arise due to the formation an inert Fe(III) or mixed Ru(IV,III)-Fe(III,II) oxide surface coating.

Objective 5. Determine the mechanism by which different Fe(II, III) oxides (possibly Fe metal) trap various forms of Ru which are transported in the vapor/aerosol phase, e.g., as RuO_4 or RuO_3 depending on different redox potential conditions in the gas streams. According to Maas and Long[4]: whereas iron oxides are very efficient at fixing different forms of Ru, the mechanism is not known and could range from the simple self-reduction reaction $RuO_4 \rightarrow RuO_2 + O_2$ where Fe is just a bystander, to active redox coupling between Ru and Fe(II, metal) and the formation of a mixed Ru-Fe phase.

Background and Significance. Ru is major fission product that is a mix of highly radiotoxic isotopes (primarily [103]Ru and [106]Ru with a half lives of 39 and 372 days, respectively) and stable isotopes.[5] Ruthenium, as [106]Ru, has been identified as one of the semi-volatile nuclides requiring the greatest degree of abatement prior to discharging the plant reprocessing off-gas to the

environment. Ruthenium can also be released during catastrophic nuclear accidents. Similar to iodine, ruthenium has a rich and complex chemistry that spans 10 accessible redox states from -2 to +8, with physical/chemical states that manifest low solubility in water and strong acids, high solubility in water, lower valent cationic species that display sharp adsorption isotherms, higher valent mobile anionic species, and the potential for efficient gas phase transport. This complexity, particularly its redox flexibility, has secured a central role for Ru in catalysis and energy storage devices. Of particular interest in the present context is the vast literature on the heterogenous catalytic and energy storage properties of ruthenium dioxide.[6] Ru chemistry is expected to be highly dynamic and strongly dependent on experimental/environmental conditions. Anthropogenic Ru enters the environment primarily in four forms:

1.) **Ru metal**: near field UO_2 fragments (e.g., Chernobyl[7]). Release during H_2 induced reactor explosion (e.g., Fukushima-Daiichi nuclear accident[8]).
2.) **$RuO_2 \cdot nH_2O$**: near field UO_{2+x} fragments (U needs to be oxidized to U_3O_7 before Ru metal oxidizes), far field condensed from $RuO_4(g)$ (release from oxidizing nuclear accident) .
3.) **$RuCl_3 \cdot nH_2O$**
4.) **Different forms of ruthenium nitrosyl or $RuNO(NO_3, OH, Cl)_3$** (purposeful/incidental release from reprocessing nuclear fuel; e.g., Sellafield[1,9,10,12];)
5.) **$RuO_4(g)$:** release into atmosphere due to oxidizing nuclear facility explosion,[6] release from reprocessing nuclear fuel[3]. Very reactive, might undergo photocatalytic reduction to $RuO_2 + O_2$,[12] or simple sorption on surfaces could catalyzes auto reduction[3,4] to $RuO_2 + O_2$. The half -life of RuO_4 at 90 °C is about 5 hours depending on other the presence of other volatiles.

Objectives 1-3 were focused on three contrasting forms of Ru: $RuO_2 \cdot nH_2O$ which is only sparingly soluble in water, ruthenium nitrosyl which is very soluble, and the volatile tetra-oxide RuO_4. Although intermolecular and valence conversion of Ru species in the catalytic and energy storage fields has a vast literature base (see above), the interaction of Ru with naturally occurring materials and in particular the potential for valence state transformations of Ru coupled to redox active elements in environmental and engineered systems has not been studied in any systematic or fundamental way. For example, in order explain the strong and recalcitrant association of Ru with iron minerals in certain natural sediments, Jones et al.[1] co-precipitated Ru (as nitrosyl) with ferric iron which yielded irreversible sorption. However, they did not perform any solid-state characterization or valence determination of the Ru/Fe end-product. It remains an open question whether Ru nitrosyl oxidized to sparingly soluble RuO_2 or possibly became incorporated into the structure of the Fe oxide precipitate as either Ru(III) or Ru(IV). $RuCl_3(aq)$ exhibits sharp adsorption isotherms from pH 3-5.7 for hematite, ferrihydrite, and magnetite where adsorption on hematite sharply decreases with increasing pH > 8 but is constant for magnetite and ferrihydrite.[13] The author's raise the possibility that Ru is incorporated into ferrihydrite whereas they suggest that magnetite suppresses the formation of more labile higher valent anionic species. However, there was insufficient characterization of the solid too arrive at any firm conclusions. That Ru can be incorporated in ferric oxides (α -Fe_2O_3) has been demonstrated in the photocatalytic literature albeit not under environmentally relevant conditions.[14-18] But even here, the valence state and local coordination environment of Ru has not been determined. An excellent study by Luxton et al.[19] demonstrated that organic reductants can reduce $RuO_2.H_2O$ but that Ru(III) is largely trapped in the solid phase indicating that the oxide can indeed act as a supercapacitor under simulated environmental conditions.
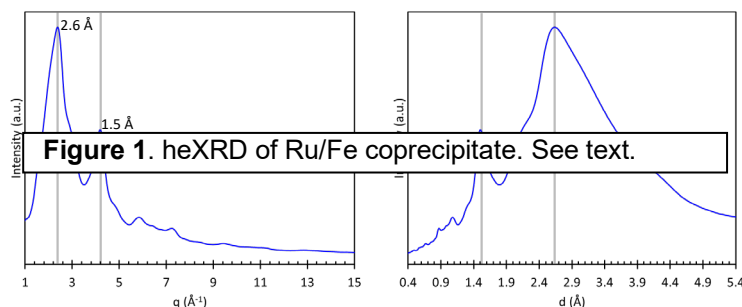
2.0   Research Design and Methodology

Experimental and Materials. All work will be performed with stable isotopes of Ru to avoid unnecessary hazards. Objectives 1 and 3 were carried out in EMSL 1410 using standard stirred batch reactors (Teflon bottles), reagent grade Fe(III, II) and Ru(III, II) salts and text book methods for synthesizing Fe (oxy)(hydr)oxides (e.g., Schwertmann and Cornell[20]). Reagent grade $RuO_2 \cdot nH_2O$ was purchased in colloidal form. Ru nitrosyl was used because it under-goes slower hydrolysis reactions than Ru chlorides. Duplicate experiments were kept under either an inert gas (glove box) or open to air. Reaction progress was tracked by systematic sampling of the suspension followed by centrifuge filtration to separate liquid and solid for characterization. The pH was monitored and titrated with a base or acid as necessary. Objective 4 was performed in the Glass Laboratory in APEL (lead Josef Matyáš). Fe functionalized aerogels were synthesized by passing ferric nitrate solutions through thiol-functionalized aerogels. The samples were then heated at different temperatures under H_2/Ar gas mixtures. Due to time and funding constraints we have not yet reached the stage of reacting the aerogels with gaseous Ru and will only report on characterization of the Fe-aerogels.

Characterization. *Solid state analysis* by XPS (chemical state, including valence of Ru and Fe, at the near-surface of solids); EXAFS/XANES (local structure around Ru and Fe, oxidation states in the bulk solid; pair distribution functions (pdf) from total scattering for both short and long range order (Ru is a good target despite possible relatively low solubility in Fe phases because has much greater scattering cross section than Fe or O); atomic resolution TEM with EDS and EELS capabilities (atomic to nanoscale distribution of Ru); SEM/EDS analysis for sub micron characterization; *Solution analysis* by ICP-OES and/or ICP-MS, Raman, UV-vis.

Simulation and modeling: Ab initio molecular dynamic (AIMD) modeling and FEFF calculations were used in combination to simulate EXAFS and PDF spectra that can serve as standards to fit experimental spectra. Such an approach will draw out important details of the local environment of the impurity component that cannot be obtained by shell-by-shell fitting of the EXAFS or guessing structures for the PDF.[21-25]

3.0   Results

Objective 1. In order to coprecipitate Fe and Ru, a starting solution of FeNO3 and RuNOCl3 was prepared at pH = 1 and Ru/(Ru + Fe) = 0.02 atom %. NaOH freshly mixed from powder stored in glove box was mixed with de-ionized water to make a stock solution at 10 M concentration which was used to titrate the Ru + Fe solution up to pH 10.5. The precipitate was characterized by high-energy X-ray diffraction (heXRD) demonstrating that co-precipitation of Ru with Fe (Ru/Fe ~ 2%) yielded 2-line ferrihydrite (Fig. 1, left panel), with only very broad features at the 2.6 and 1.5 Å peaks. The same data, but showing the d-spacing rather than q, is shown in the right panel of

Figure 1. heXRD of Ru/Fe coprecipitate. See text.

Figure 1. The peaks commonly associated with 3- and 6-line ferrihydrite, primarily between 2.6 and 1.5 Å, only show up as broad shoulders to the two main peaks.
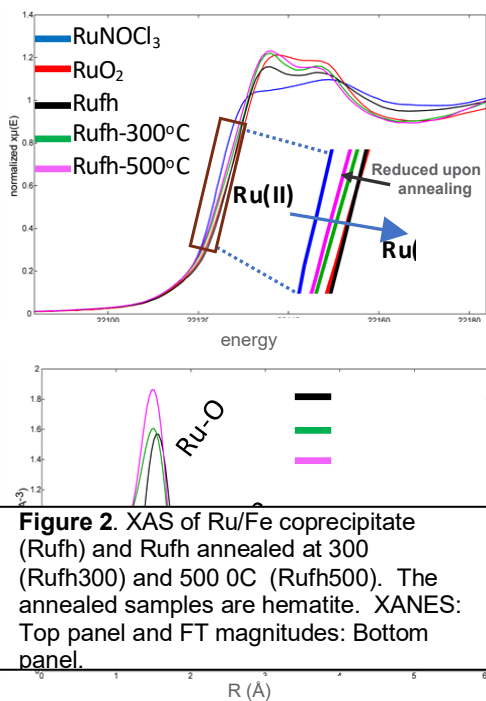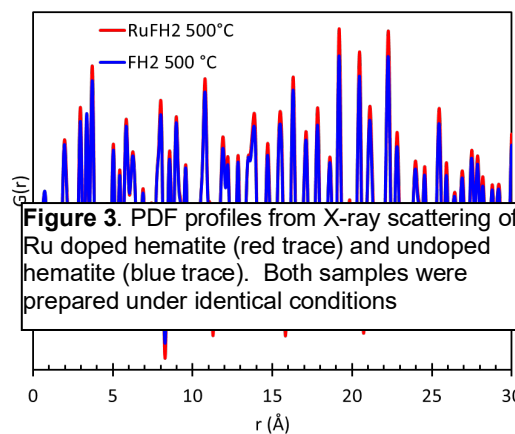
Figure 2. XAS of Ru/Fe coprecipitate (Rufh) and Rufh annealed at 300 (Rufh300) and 500 0C (Rufh500). The annealed samples are hematite. XANES: Top panel and FT magnitudes: Bottom panel.

XANES (Fig. 2, top panel) clearly demonstrates that Ru associated with ferrihydrite (fh) is in the +4-oxidation state. Because Ru was initially divalent (i.e., $Ru^{2+}NO^{+}Cl_3$), Ru oxidized during coprecipitation. Further, the results were the same whether the experiment was performed under anoxic or oxic conditions, strongly suggesting that Fe(III) oxidized Ru in Ru nitrosyl. Unfortunately, the amount of Fe(II) produced was too low to detect. The Fourier transform data (Fig. 2, lower panel) shows a strong second shell peak at ~ 2.9 Å, after phase correction, which is likely a Ru-Fe atomic distance, which might imply incorporation of Ru(IV) into the structure of fh. However, given the uncertainty and controversy surrounding the fh structure, it is difficult to arrive at an unambiguous conclusion.
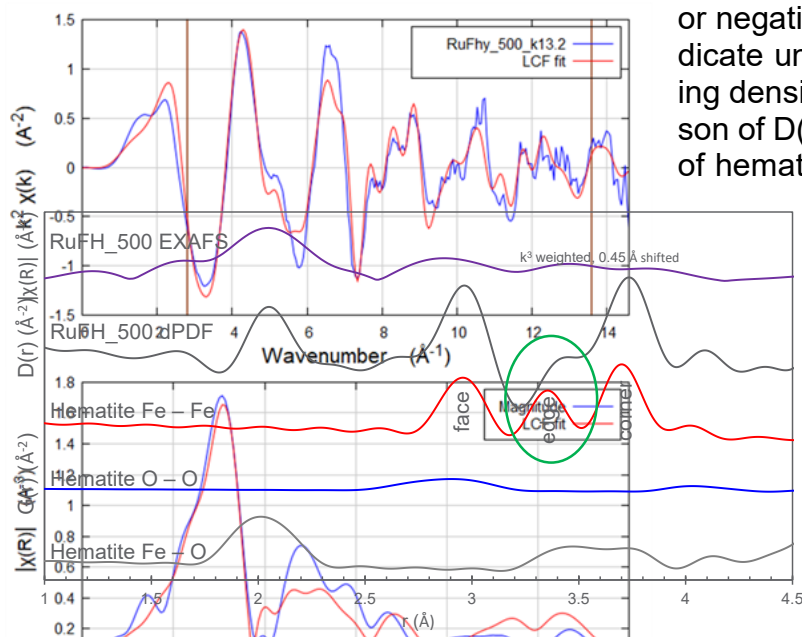
A second set of experiments were initiated whereby Ru nitrosyl was interacted with preformed hematite. Although adsorption occurred, interpretation of the Ru oxidation state by XPS is uncertain because of interference of a main Ru energy level with the C 1s line that hindered calibrating the energy scale. Here we need more standards to deconvolute the signals and/or gain more time at the APS to perform XANES.

Objective 2. Rufh (Ru-ferrihydrate formed by coprecipitation) was annealed at 300 and 500 °C in air for 14 hours to simulate conditions commonly used for doping hematite with Ru for improved photocatalytic performance. We also note that fire events in Nature can often reach 500-600 °C at the near surface of a soil profile. We shall only discuss the 500 °C results as the 300 °C results have proven difficult to understand. Comparison of the PDF profiles (Fig. 3) of undoped hematite (FH500) and doped hematite (RuFH500) shows the structures of the two materials are nearly identical, with the exception that all peaks corresponding to iron atom pairs are more intense for RuFH500 (i.e., Ru is a stronger scatterer than Fe or O). This indicates that Ru likely substitutes for Fe in the hematite structure. This is consistent with the FT magnitudes in Fig 2 (bottom panel) that show strong amplitudes where one would expect Ru-Fe distances corresponding to face-, edge- and corner-sharing octahedra of hematite. As determined by the Rietveld fit (not shown), the

Figure 3. PDF profiles from X-ray scattering of Ru doped hematite (red trace) and undoped hematite (blue trace). Both samples were prepared under identical conditions
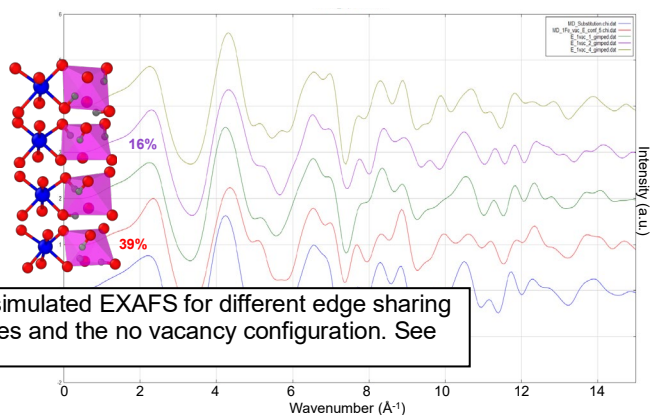
lattice parameters are almost identical between FH500 and RuFH500 and the peaks line up in the PDF well beyond the short-range order. The differential PDF (Fig. 4, second

spectrum from the top) is the difference $G(r)_{RuFH500} - G(r)_{FH500}$ and represents the Ru-induced difference in structure between the two samples. For example, any peaks in the differential PDF correspond to atom pairs where Ru has substituted for Fe. Absent peaks or negative peaks, on the other hand, indicate unchanged or diminished scattering densities due to vacancies. Comparison of D(r) to the calculated partial PDFs of hematite Fe – Fe, O – O, and Fe – O atom pairs reveals that the Fe – Fe distances between edge-sharing octahedra (3.35 Å) are most affected by Ru incorporation. This indicates Ru incorporation is likely coupled with an iron vacancy in an edge-sharing site. Ru K-edge XANES measurements show Ru is likely in the 3+ oxidation state (Fig. 3, top panel), which means the iron vacancy needs to be compensated by three protons or a proton and an oxygen vacancy. The iron vacancy likely occurs to accommodate the larger Ru cation – note the longer Ru – O distance in the D(r) compared to the hematite standard. This information is key for narrowing the search of configuration space for ab initio molecular dynamics (AIMD) informed EXAFS, which will be discussed next.

Figure 4. Difference between PDFs of undoped and Ru doped hematite given by grey trace compared to PDFs of undoped hematite. See text for details.

Armed with the knowledge that Ru is likely associated with a protonated Fe vacancy(s) at edge sharing sites we performed AIMD simulations on Ru configurations that contained such defects. Note that whereas there are 3 identical edge sites per Ru (Fe), there are 20 ways to rearrange the protons. Of these 20 we chose 4 with the lowest 0K energies and one configuration with no vacancy. The resulting simulated EXAFS are shown in Figure 5 and used in linear combination fits to the experimental data. It is apparent that the position of the protons does influence the EXAFS spectra, indicating that this is indeed an important parameter to constrain (Figure 5). The best fit to the data yields 45% weight to the no vacancy configuration and 55 % weight to a combination of two distinct protonated Fe vacancy configurations (Fig. 6). This is a remarkably good fit for such a narrow search of configuration space and confirms the likely presence of local protonated Fe vacancies at edge-

Figure 5. AIMD simulated EXAFS for different edge sharing protonated Fe sites and the no vacancy configuration. See text.

sharing sites. The near perfect match to the first shell Ru-O peak at around 1.6 A, un-phased corrected, (Fig. 6, bottom panel) indicates that coupled O-Fe vacancies are un-likely. The underestimate of peak amplitudes for Ru-Fe distances between ~2.4 and ~3 Å (un-phase corrected) possibly indicates we are missing a configuration(s) as the configurations used likely overestimated the thermal disorder for Ru-Fe atomic pairs. We note that there is no guarantee that lower energy configurations will dominate. The excess amplitude at ~5 Å is likely due to correlated motions imposed by the periodic boundary condition. This could be overcome by using a larger unit cell, but the costs rapidly become prohibitive.

Objective 3. Experiments with $FeCl_3$(aq) and $RuNOCl_3$(aq), the homogeneous system, at Ru^{2+}/Fe^{3+} = 100 mM/180 mM and pH = 3, showed redox activity; UV-vis, using the ferrozine method, indicated ~3 % and ~5 % of total Fe^{3+} was reduced to Fe^{2+} after 1 hour and 1 week of reaction, respectively. However, FTIR indicated that $Fe^{2+}NOCl_3$ was formed. Indeed Fe^{2+} can π-bond with NO. Consequently, the degree of Fe^{3+} reduction might have been underestimated by the UV-vis method.

Objective 4. In contrast to prior objectives, here Ru is initially in the solid state as RuO_2 and Fe is in solution as Fe^{2+}. Conditions were pH = 3, Fe^{2+}(aq) = 179 µM, and 75 µM RuO_2. A range of potential reactions are illustrated in Figure 7. The expectation was for Fe^{2+} to reduce Ru^{4+} to $Ru^{3+/2+}$ and for the resulting Fe^{3+} to plate out on the surface of RuO_2. Initial results were somewhat surprising in that XPS analyses showed that both

**Figure 6**. Best fit to Rufh500 XAS. See text for details.

Fe(III) and Fe(II) at the surface with Fe(II) in excess of Fe(III) (Fig. 8). As the experiments were performed at pH 3 and the solids rinsed in pH 3 deionized water after the

experiments we did not expect to see Fe(II) at the near surface of RuO_2. It is possible that Fe(II) was incorporated into

Figure 7. Schematic showing possible reactions between Fe^{2+}(aq) and RuO_2(s)

Figure 8. XPS of RuO_2 reacted with Fe^{2+}(aq) fit with Fe(III), smooth red line, and Fe(II), green line, standards..

the solid phase, but other tests will be required to vet this possibility. We note that the very low concentration of Fe at the surface of RuO_2 precludes detecting any reduced Ru with XPS. Solutions are awaiting analyses.
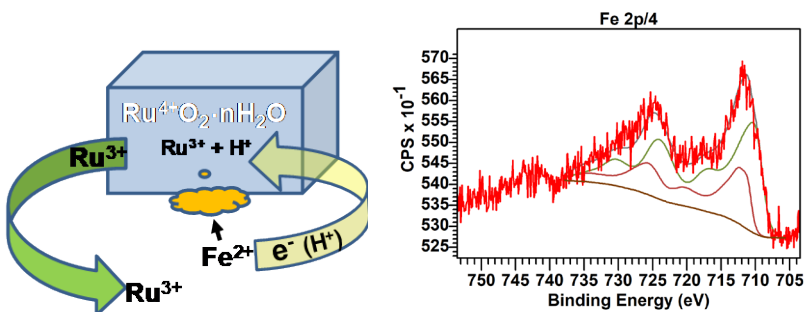
Objective 5. Fe functionalized Si aerogels were synthesized as described in the Experimental section and illustrated in Figure 9. SEM/EDS (not shown) showed that Fe was distributed homogeneously at the submicron scale with no detected precipitates. XPS analysis gave Fe/Si atom ratios = ~1%. XPS analysis of the Fe2p line for the sample as is indicated about Fe(II)/Fe(III) = 62%. The sample treated with 2.5% H_2/Ar at 225 ^oC showed a slight increase in Fe(II) where Fe(II)/Fe(III) = 70% but no detectable Fe metal (Figure 10). We posit that thiol partially reduced Fe^{3+} during the initial impregnation step as XPS indicates there is excess sulfate present (not shown). The high binding energy for the Fe(II) component (~711 eV) strongly suggests that Fe(II) is bound to Si-O terminations. Higher T sample prep and Ru(gas) capture tests are pending.
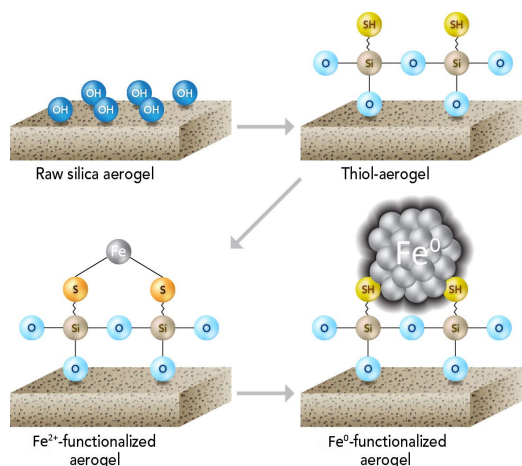
Figure 9. Schematic showing steps for functionalizing the Si-aerogels with Fe
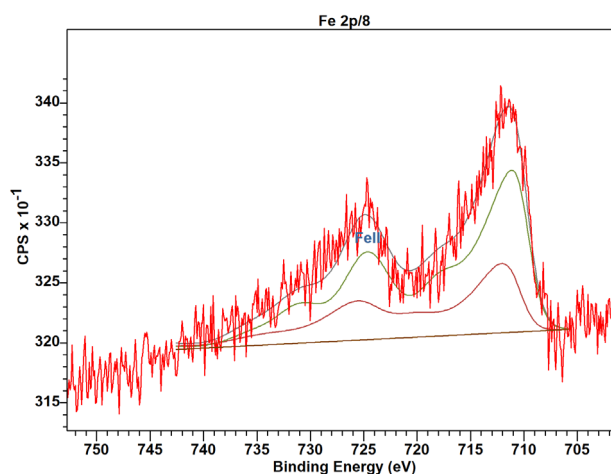
4.0 Conclusions

$RuNOCl_3$ and Fe^{3+} are redox active over a broad range of pH. Initial assessment of effect of redox coupling between Ru and Fe indicates that Fe(III) in ferrihydrite can oxidize Ru^{2+} in $RuNOCl_3$ to Ru(IV) during coprecipitation at ambient conditions and alkaline pH. Further, evidence suggests that Ru(IV) is incorporated in the structure of fh. Likewise, Fe^{3+}(aq) also reduces Ru^{2+} in $RuNOCl_3$ in the homogenous system at acidic pH although the kinetics of reaction appear to be slow. Rufh annealed to 500 ^0C transforms to Ru(III) doped hematite. AIMD informed EXAFS indicates that Ru substitutes for Fe(III) in regular octahedral sites of hematite but requires three distinct configurations involving edge-sharing protonated Fe vacancies and straight substitution with no local defects. Fe^{2+}(aq) appears to oxidize at the surface of RuO2, but the amount is too low to reasonably expect detectable reduced Ru. Future experiments at higher pH are warranted to make Fe^{2+}(aq) less stable (i.e., make more redox active). We also demonstrated that we can functionalize Si aerogels with Fe(II) and Fe(III) but likely need to go to higher T to make Fe^o nanoparticles.

5.0 References

1   Jones, R. F. THE ACCUMULATION OF NITROSYL RUTHENIUM BY FINE PARTICLES AND MARINE ORGANISMS. *Limnology and Oceanography* **5**, 312-325, doi:10.4319/lo.1960.5.3.0312 (1960).

2   Hansel, C. M., Benner, S. G. & Fendorf, S. Competing Fe(II)-induced mineralization pathways of ferrihydrite. *Environ. Sci. Technol.* **39**, 7147-7153 (2005).

3   Mun, C., Cantrel, L. & Madic, C. Review of literature on ruthenium behavior in nuclear power plant severe accidents. *Nuclear Technology* **156**, 332-346, doi:10.13182/nt156-332 (2006).

4   Maas, E. T. & Longo, J. M. CONFINEMENT OF RUTHENIUM OXIDES VOLATILIZED DURING NUCLEAR-FUELS REPROCESSING. *Nuclear Technology* **47**, 451-456, doi:10.13182/nt80-a32399 (1980).

5   Zuba, I., Zuba, M., Piotrowski, M. & Pawlukojc, A. Ruthenium as an important element in nuclear energy and cancer treatment. *Applied Radiation and Isotopes* **162**, doi:10.1016/j.apradiso.2020.100176 (2020).

7   Over, H. Surface Chemistry of Ruthenium Dioxide in Heterogeneous Catalysis and Electrocatalysis: From Fundamental to Applied Research. *Chemical Reviews* **112**, 3356-3426, doi:10.1021/cr200247n (2012).

8   Krouglov, S. V., Kurinov, A. D. & Alexakhin, R. M. Chemical fractionation of Sr-90, Ru-106, Cs-137 and Ce-144 in Chernobyl-contaminated soils: an evolution in the course of time. *Journal of Environmental Radioactivity* **38**, 59-76, doi:10.1016/s0265-931x(97)00022-2 (1998).

9   Abrecht, D. G. & Schwantes, J. M. Linear Free Energy Correlations for Fission Product Release from the Fukushima-Daiichi Nuclear Accident. *Environ. Sci. Technol.* **49**, 3158-3166, doi:10.1021/es5053733 (2015).

10   Livens, F. R. & Baxter, M. S. PARTICLE-SIZE AND RADIONUCLIDE LEVELS IN SOME WEST CUMBRIAN SOILS. *Science of the Total Environment* **70**, 1-17, doi:10.1016/0048-9697(88)90248-3 (1988).

11   Livens, F. R. & Baxter, M. S. CHEMICAL ASSOCIATIONS OF ARTIFICIAL RADIONUCLIDES IN CUMBRIAN SOILS. *Journal of Environmental Radioactivity* **7**, 75-86, doi:10.1016/0265-931x(88)90043-4 (1988).

12   Caborn, J. A., Howard, B. J., Blowers, P. & Wright, S. M. Spatial trends on an ungrazed West Cumbrian saltmarsh of surface contamination by selected radionuclides over a 25 year period. *Journal of Environmental Radioactivity* **151**, 94-104, doi:10.1016/j.jenvrad.2015.09.011 (2016).

13   Zimmerman, G. L., Riviello, S. J., Glauser, T. A. & Kay, J. G. PHOTOCHEMICAL DECOMPOSITION OF RUO4. *Journal of Physical Chemistry* **94**, 2399-2404, doi:10.1021/j100369a039 (1990).

14   Music, S. ADSORPTION OF MICROAMOUNTS OF RUTHENIUM ON HYDROUS IRON-OXIDES. *Journal of Radioanalytical and Nuclear Chemistry-Articles* **109**, 495-506, doi:10.1007/bf02037890 (1987).

15   Elouafi, A. *et al.* Effects of Ru doping and of oxygen vacancies on the optical properties in alpha-Fe2O3 powders. *Applied Physics a-Materials Science & Processing* **126**, doi:10.1007/s00339-020-3385-z (2020).

16   Ouertani, B., Bidouk, G., Ouertani, R., Theys, B. & Ezzaouia, H. Effect of the ruthenium incorporation on iron oxide phases synthesis, Fe2O3 and Fe3O4, at low annealing temperature. *Materials Chemistry and Physics* **242**, doi:10.1016/j.matchemphys.2019.122272 (2020).

17   Ndlangamandla, C. L., Bharuth-Ram, K., Ngom, B. D. & Maaza, M. Synthesis of Ru doped hematite nanorods for application as photo-anode material in a photoelectrochemical cell (PEC). *Hyperfine Interactions* **238**, doi:10.1007/s10751-016-1380-8 (2017).

18   Pan, H. J., Meng, X. Y., Cai, J. J., Li, S. & Qin, G. W. 4d transition-metal doped hematite for enhancing photoelectrochemical activity: theoretical prediction and experimental confirmation. *RSC Adv.* **5**, 19353-19361, doi:10.1039/c4ra12825g (2015).

19   Guo, X. L., Wang, L. L. & Tan, Y. W. Hematite nanorods Co-doped with Ru cations with different valence states as high performance photoanodes for water splitting. *Nano Energy* **16**, 320-328, doi:10.1016/j.nanoen.2015.07.005 (2015).

20   Luxton, T. P., Eick, M. J. & Scheckel, K. G. Characterization and dissolution properties of ruthenium oxides. *Journal of Colloid and Interface Science* **359**, 30-39, doi:10.1016/j.jcis.2011.03.075 (2011).

21   Schwertmann, U. C., R.M. *Iron Oxides in the Laboratory; Preparation and Characterization*. (Wiley-VCH, 2000).

22   Bylaska, E. J. *et al.* Association of Defects and Zinc in Hematite. *Environ. Sci. Technol.* **53**, 13687-13694, doi:10.1021/acs.est.9b04323 (2019).

23   Soltis, J. A. *et al.* Can mineral growth by oriented attachment lead to incorporation of uranium(vi) into the structure of goethite? *Environmental Science-Nano* **6**, 3000-3009, doi:10.1039/c9en00779b (2019).

24   Kerisit, S., Bylaska, E. J., Massey, M. S., McBriarty, M. E. & Ilton, E. S. Ab Initio Molecular Dynamics of Uranium Incorporated in Goethite (alpha-FeOOH): Interpretation of X-ray Absorption Spectroscopy of Trace Polyvalent Metals. *Inorganic Chemistry* **55**, 11736-11746, doi:10.1021/acs.inorgchem.6b01773 (2016).

25   McBriarty, M. E. *et al.* Iron vacancies accommodate uranyl incoprôration into hematite. *Environ. Sci. Technol.* (2018).

26   McBriarty, M. E. *et al.* Trace Uranium Partitioning in a Multiphase Nano-FeOOH System. *Environ. Sci. Technol.* **51**, 4970-4977, doi:10.1021/acs.est.7b00432 (2017).

3.0 Construction and modeling

The chamber and port connections were custom-made of 304L alloy steel by Kurt J. Leskar, Inc. The chamber design and associated instrumentation is shown in Figure 1.
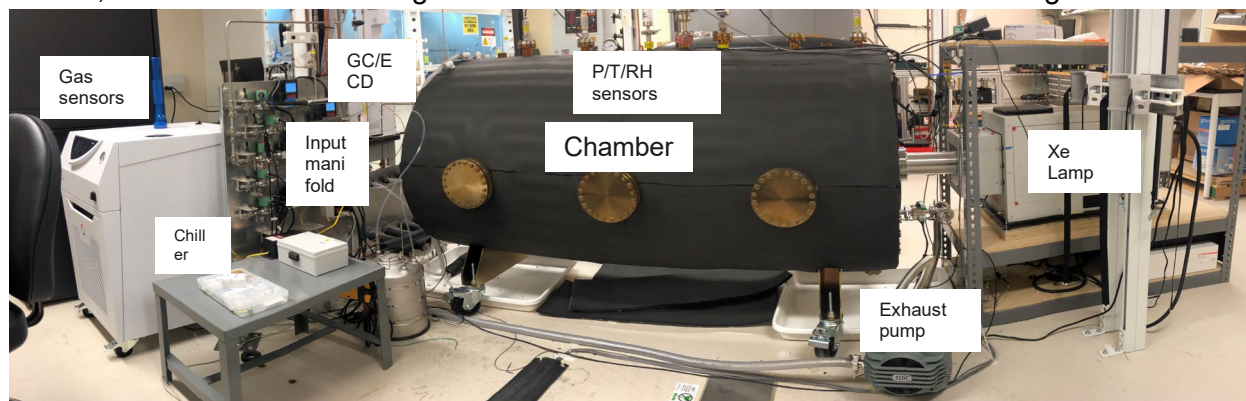

The chamber is pictured in Figure 3A and the inner volume in Figure 3C. The inner surface was lapped to a roughness (Ra) of about 0.6 microns. Twenty-six Conflat (CF) flanged ports were welded to the circular faces and along the top of the chamber, with a drainage port installed in the bottom. CF ports were chosen for their superior sealing properties and their ability to withstand exposure to the corrosive gases that are likely to be produced from iodine photooxidation. Non-metal surfaces are minimized and largely limited to valve seals. The circular face ports were installed off-axis to promote gas mixing; the only on-axis port was used to illuminate the chamber air volume. All ports were sealed or plumbed to equipment to provide a leak-tight environment for the introduction of radioactive gases and suspensions.

The chamber was instrumented with two temperature/humidity sensors (Rototronics model HC2-IE302) at opposite ends of the chamber, redundant pressure monitoring (MKS model 722B Baratron and model 910 DualTrans), and gas lines for supply, sampling, and exhaust. All gas lines are valved as close to the interior chamber as possible to provide minimal excess surface area and dead space in the vessel. The chamber can reach a vacuum of 5×10^{-4} Torr by sole use of a scroll pump (Edwards model nXDS15i). Hydroformed Hydra~Cool^2 cooling channels piped to a Lauda Variocool VC 3000 chiller with Dynalene HC-30 heat transfer fluid, provide temperature control for the chamber and is able to maintain a wall temperature between -5 °C and 80 °C under the thermal load of the light source and temperatures from -15 °C to 80 °C without the light source. This cooling system is necessary as utilizing the light source without any active cooling leads to wall temperatures exceeding 50 °C on the end faces of the chamber. The illumination source used was a 2.5 kW xenon XBO lamp (XE2500, SKU: 650-0102) (Osram, 2016) in a custom housing made by Science Tech, Inc. The lamp was attached to the chamber by use of a "light pipe" (10 cm dia., 23 cm long), 6 in. CF flanges, and a fused silica window (Kurt J. Leskar Inc. VPZL-600Q) placed on the center axis of the chamber body. The internal optics of the reflector in the lamp housing were constructed such that the light was

focused to the center of the light pipe and at such an angle as to miss the flanges with direct irradiance (a half angle of 23.3°).

The chamber allows a wide variety of gases to be introduced and mixed. The gas flow path diagram is shown in Figure 2. The primary gas is air purified by a column that removes hydrocarbons, NO_x, moisture and a limited amount of CO_2. Other non-reactive gases can be introduced using mass flow controllers. Ozone can be generated from the purified air using ultra-violet radiation generated by the lamp. The humidity in the chamber can controlled by an external heated, connected canister. Reactive gases (iodine, methyl and butyl iodide) can be introduced into the chamber using a fume hood injection system.

Figure 2: Gas flow supply pathways
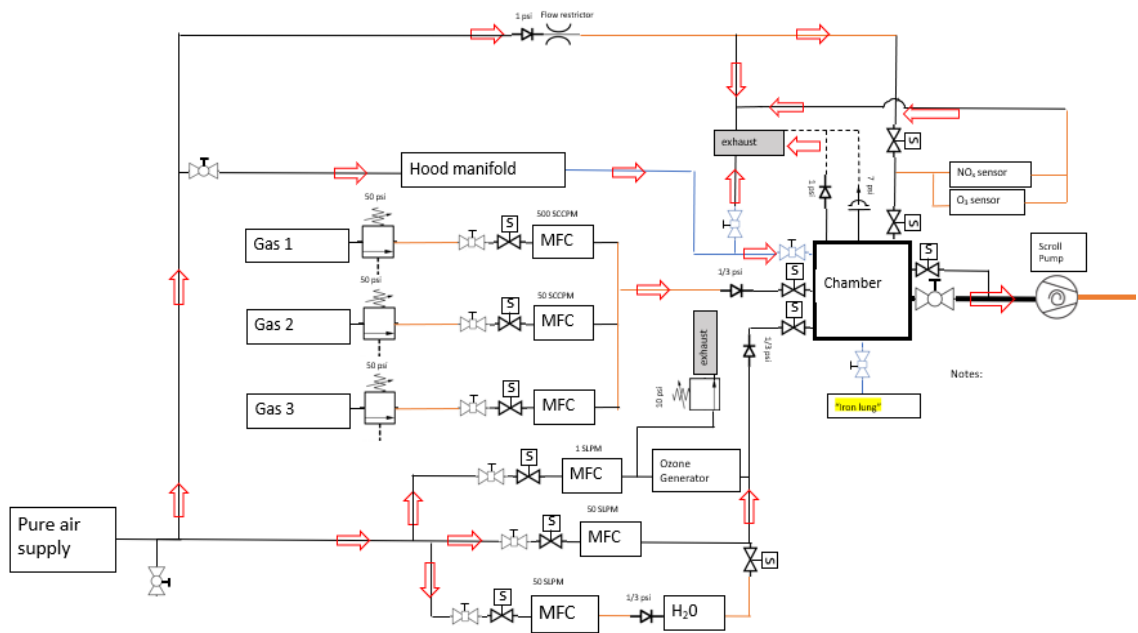
To passivate the surface to reduce wall losses and adsorption of reactive compounds as much as possible, a SilcoNert inert amorphous silica-based coating made by chemical vapor
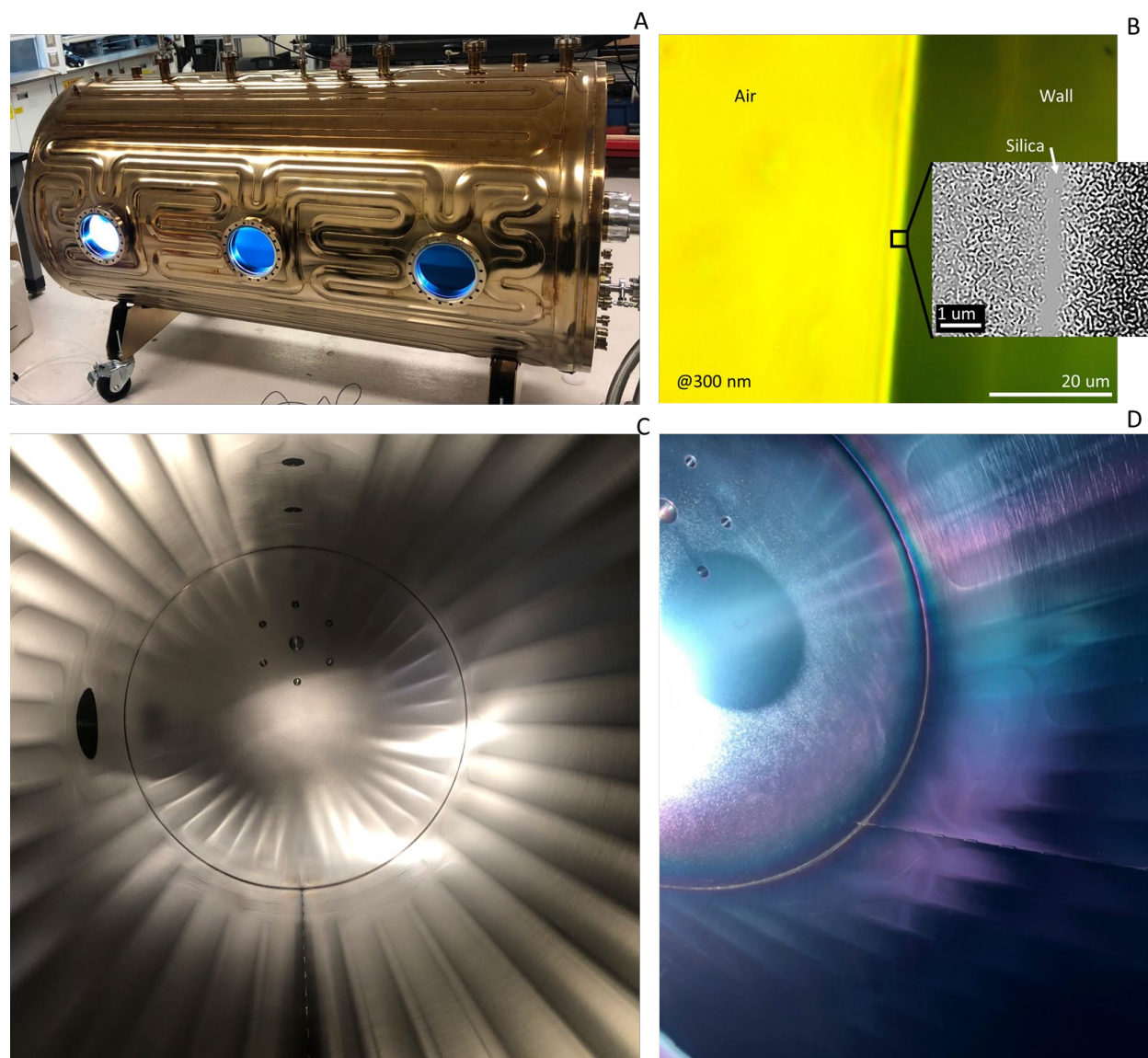

Figure 3: (A) Photograph of the exterior of the chamber prior to sealing of the access ports. (B) A 10 kX UV micrograph of the inside edge of a gasket silica coated with the chamber wall. The cutout shows the silica layer brought out with a 3 pixel Mexican-hat optical filter. (C) A photograph of the inside of the chamber with a steel wall taken prior to silica coating, the photo is taken from the middle access port facing side of the chamber opposite the light pipe. (D) A photograph of the area in the chamber as (C) after silica coating, the photo is taken from the access port seen on the left of (C).

deposition (CVD) was deposited onto the interior surfaces by SilcoTek Corporation (SilcoNert 2000, seen in Figures 3B & D) and capped with a proprietary organic capping agent. As workpieces this large are uncommon, the silica coating thickness was unknown until the chamber was opened and inspected at Pacific Northwest National Laboratory, Figure 3B. The modeling effort spanned the anticipated thickness range to provide a model to account for

thickness variations in corners as well as variability in the final film that may form if the process was reproduced.

3.1 Optical Modeling

The optical modeling had the following goals.

- Seek to understand the effective optical constants and reflectance of the wall materials.
- Provide a detailed three-dimensional rendering of the inner chamber for illumination calculations.
- Combine a light source, the obtained reflectance, and the inner chamber to determine the amount of optical energy from the direct illumination and the integral illumination from reflected light by the chamber walls.

The initial optical constant modeling determined the effective optical constants (n and k) using CompleteEASE version 3.65 with the standard optical packages. For the models, the steel chamber wall was assumed to be an infinite absorber, with surface oxide and pure silica layers added onto it. The roughness of the wall was experimentally determined by comparison to a commercial surface finish standard for lapped and polished metals (Destiny Tools, Inc., 2021). The effective optical constants were simulated for wavelengths from 200 to 1800 nm and from angles of 1 to 89 degrees.

The resultant optical constant data were averaged over three distinct wavelength regions: ultraviolet (UV) at 200-400 nm, visible (Vis) at 400-700 nm, and near infrared (NIR) at 700-1800 nm. This averaging helped to gain an understanding of the overall influence of the chamber walls on the chamber illumination. The averaged optical constants were converted to reflectivity by the method in Kasap and Capper, 2017. The effective reflectivity for each modeled case was then employed for optical illumination modeling.

3.2 Inner Volume Rendering

AutoCAD version 2017.1.2 (N.402.0.0) was used to create a three-dimensional rendering of the inner chamber volume. The chamber was made to scale, with a 91.5 cm (3 ft) inner diameter and 182.9 cm (6 ft) length, with accurate port placement and sizing (for experimental measurement predictions from the ports). A reflector panel was placed at the end of the light pipe in lieu of a lamp body. The chamber was then rendered to a resolution factor of 10 (MINRES = 10) and exported to AGI-32 for illumination modeling.

3.3 Illumination Modeling

The results of the previous two modeling efforts were loaded into AGI-32 version 18.3.2, for illumination analysis. The first step in the modeling was to import the three-dimensional rendering of the chamber. The rendering was then sliced down the center axis for internal investigation and if needed, a perfect mirror was used to cover the central axis of symmetry. Each individual wall face from the ports/caps, to the steel chamber wall, and the light pipe were given the applicable reflectance for the simulation based on the results of the optical constant

modeling. The rendering's mesh level was set to 3.2, ~8.8e6 mesh elements. With the three-dimensional rendering loaded with the correct reflectance, a light source was added to the model.

The illumination source was modeled with a point source placed at the center of the light pipe along the center axis and given the same emission angles as the optics of the XBO lamp in its housing. Measurements of the lamp intensity (taken with Newport 818-UV sensor) were used to inform the illumination source, along with standardization of intensity to conform to Michael (2019). With the light source and chamber characterized and meshed, simulations were run under varying the reflectivity characteristics of the chamber wall's coating.

3.4 Characterization Tools and Parameters

A power radiometer was used to measure the intensity of the light and verify the model results. The measurements were done with a Newport 818-UV and associated single channel data collection, and recorded with PMManager version 3.31. Optical power intensities were calculated from the detector by means of vendor supplied calibration curves. The mean and standard deviation were collected at each measurement point. The power intensities from the radiometer were also accompanied by spectral measurements.

The light spectra within the chamber were recorded with an Ocean Optics Flame model UV-Visible grating spectrometer. A 10 ft, 1 mm diameter patch cord with SMA ends and a collimating lens (Ocean Insights 74-VIS, set at 0.5 cm from lens) were used to collect the light. The data were recorded with OceanView version 2.0.7 with an integration time of 6-100 ms (to maximize the signal), 10 averaged spectra, and a box car averaging set to 0.

3.5 Measurement Conditions

Both the power and spectrum were recorded with the illumination source at 100 percent power (2.5 kW). The lamp had an electrode post that cast a small shadow in the chamber, which is not accounted for in the modeling. During the optical measurements, 10 SLPM of clean air was piped into the chamber to maintain a clean environment and to minimize any external dust coming into the chamber.

4.0 Results and discission

The maximum optical power measured at the fused silica window of the light pipe was 646 ± 6 W. The chamber's cross-section was 0.65 m^2, making the average power density by cross section 985 ± 8 W/m^2, which corresponds well to the current solar standards (Hulstrom et al., 1985; Michael, 2019) of 875-1050 W/m^2. A comparison of the lamp's power spectrum to solar spectra at air mass (AM) 0-1.5, (Hulstrom et al., 1985; Michael, 2019), can be seen in Figure 4A.

The results of the direct illumination of the air mass calculation can be seen in Figure 4B. The direct illumination is reflected based on the optical properties of the chamber walls (effective n, <n> shown) in Figure 4C. The combination of the direct illumination and reflected intensity allows for the calculation of the optical intensity within the chamber.

Figure 4D presents a summary of the reflected light intensity as a function of wall coating and wavelength range. The results are ordered on the vertical axis by the thickness of the silica coating from 0 to 325 nm and on the horizontal by wavelength range (UV = 200-400 nm, Vis = 400-700 nm, NIR = 700-1800 nm).

The optical power intensity was measured before and after the SilcoNert coating was applied to the chamber walls. The optical intensity measured at each port and inside the air mass appeared to vary by about 5 percent. This was attributed to vibration in the gantry built to hold the sensor and lines as seen in intensity variations during short time scales depending on the configuration of the sensor support structure. In Figures 5A and B, select intensities at the chamber wall and within the chamber volume are reported. The values next to ports were taken at the mouth of the chamber air mass, the large blocks indicate the wall intensities integrated to account for all the light reflected into the sensor (i.e. measurements with the sensor orientated towards the far wall), and the arrowed values report the maximum intensity measured directly in the air mass itself with the arrow signaling the direction of the sensor face. Figures 5A and B report the intensity measurements as the percent of the maximum measured intensity and are for the steel wall and silica-coated wall respectively.

Figure 5C is a comparison of the spectra of the chamber before and after the chamber was coated with the SilcoNert coating. The light in both figures was introduced from the right of the image through the light pipe. Both represent the average spectrum taken from the same measurement locations within the chamber. The results were averaged to represent an overall spectrum of the chamber.

This work involves the description of the light intensity within the air volume of the atmospheric radioisotope chamber. Previous work (Pareek et al., 2008; Romero et al., 1997; Huang et al., 2011; Elloumi et al., 2002) report on exhaustive research on how to best integrate the models described in Figures 5A and B for gases only, fine particles, and how to treat the intensity at any ports or fine features of the atmospheric radioisotope chamber.
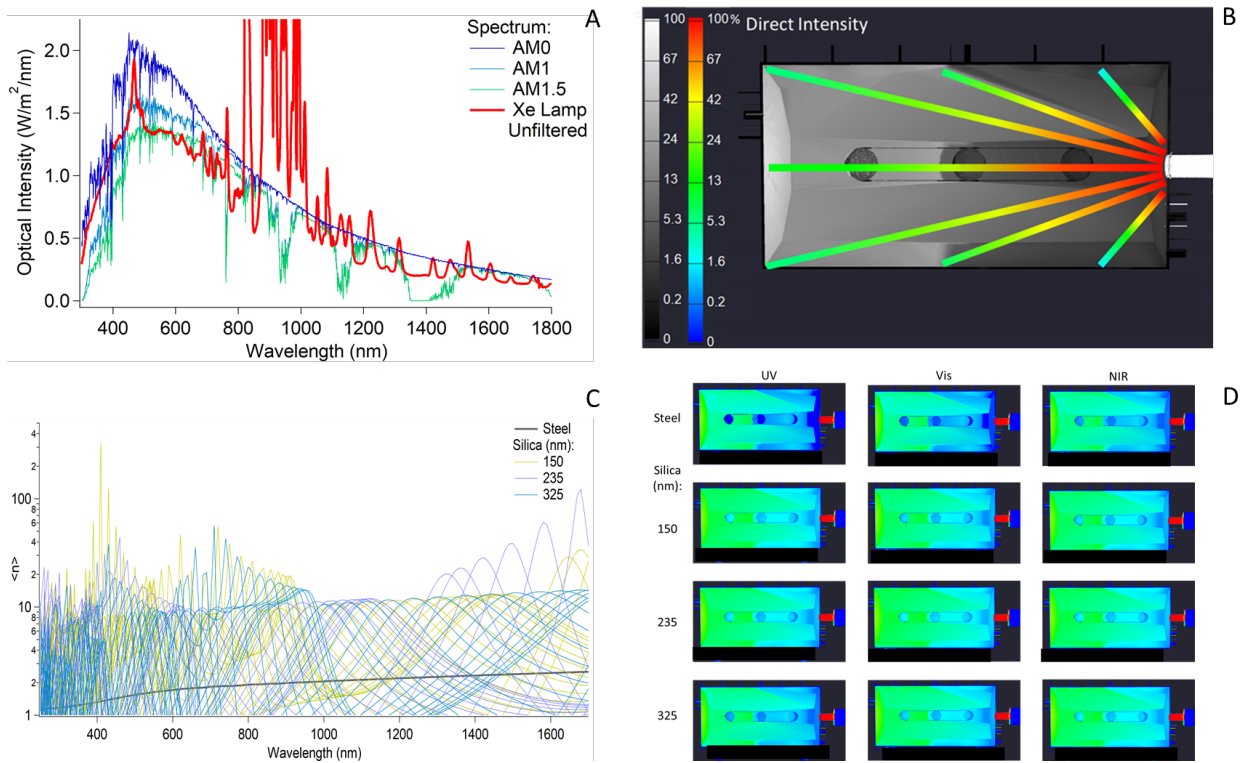
Figure 4: (A) The spectrum of the xenon lamp compared to the spectra for air mass (AM) 0-1.5. (B) Direct intensity guidelines showing optical intensity in the chamber air mass. (C) The refractive index of the inner surface of the chamber wall from a silica thickness of 0 (steel) to 325 nm. The data are simulated from 0 to 90 degrees by steps of 5 degrees. (D) Example Optical Intensity modeling results as a function of silica wall coating thickness (rows) and light wavelength (columns).
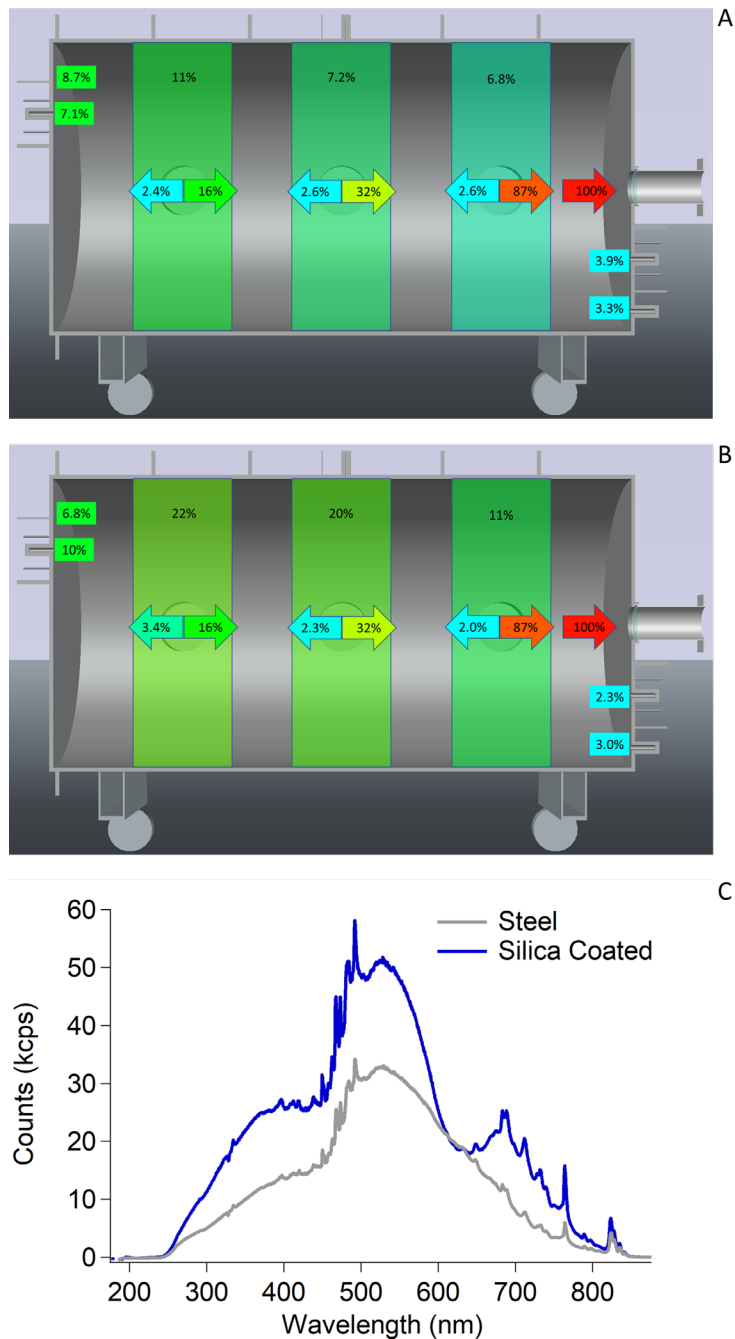
Figure 5: (A) Compiled intensity power measurements of the light at various points in the chamber before the walls were coated with silica. All values are relativized to the maximum intensity measured at the inlet silica window, of 646±6 W/m2. (B) Compiled intensity measurements of the light in the chamber after SilcoNert coating of the inner surfaces. (C) Average chamber light source spectra for different chamber wall material.

As the light source is introduced at one end of the chamber with a focal length much shorter than the length of the chamber, the largest portion of the optical irradiance comes from direct intensity of the lamp. The second portion comes from the intensity reflected off any surface directly opposing the direct intensity of the lamp (i.e., the opposing wall of the chamber), and lastly by integration of intensity perpendicular to the axis of the chamber (i.e. the cylindrical wall of the chamber). According to Elloumi et al. (2002), integration of these light sources will enable direct calculation of the irradiance at any finite point within the chamber. As the conditions for the light intensity will change with experimental conditions (e.g., fine particles scattering the light versus gas-only chemistry), the exact integration method may change, but the results in Figures A and C can be used to calculate the wall reflection component of the light intensity.

Figures 4B and D represent the results of such modeling for a case in which the chamber is filled with clean air to demonstrate the utility of the model. The intensities reported in Figures 4B and D are the average for each individual mesh element. These intensities are equivalent to the configuration factors in), whose summation accounting for angle, distance, and air absorption factors allows for integration of the light intensity for any given point in the internal air volume.

Figures 5A and B corroborate the model results presented in Figures 4B and D. The measured light intensity matches the model within the given error of the measurement for each wall section as well as each port. For a clean air case, the results of the model concur with the experimental measurements.

Figure 4C further corroborates the modeling efforts. The calculation of the effective optical constant ($<n>$) in Figure 4C shows that for most angles, SilcoNert coating of the chamber wall enhances the light intensity in the 300 to 400 nm and 500 to 600 nm regions if the average silica thickness ranges is 200 -250 nm. The slight enhancement of visible light from 630 to 800 nm is indicative of films from 235 to 325 nm. Figure 3B, shows a UV micrograph of the silica layer in which the thickness varies from 200 to about 350 nm. The experimental measurements corroborate the optical modeling and correlate to the measured intensity enhancement upon silica coating the chamber wall.

5.0 Conclusions

Optical modeling provides the data necessary to evaluate the total optical radiation incident on chamber gases by using models of the optical intensity inside an optical chamber at any given point. In experiments where optical irradiance is a rate-limiting factor for photocatalytic reactions, this model will clearly enable a means to improve the interpretation of experimental results and assist in the translation of experimental data into an atmospheric model. Direct measurements of optical intensity are well corroborated by optical modeling, providing validation of the optical model used. Further analysis of chamber characteristics including wall reactivity (wall losses) and flow modeling is ongoing and will be reported in future work.

6.0 References

Becker, E. M., M. J. Myjak, A. M. Prinke, W. J. Kernan, and S. G Homann, 2021: Evaluation of an airborne alpha and beta particle detection capability using an environmental continuous air monitor system. *Journal of Environmental Radioactivity*, 228, 106527. (Becker et al., 2021)

Destiny Tools, Inc., 2021. "Understanding Surface Finish." Destiny Tool Product Tutorial. 2021. https://www.destinytool.com/surface-finish.html

Elkhatib, H., M. A. Awad, and M. A. El-samanoudy, 2021: Progress in Nuclear Energy Modeling of Atmospheric Dispersion and Radiation Dose for a Hypothetical Accident in Radioisotope Production Facility. *Progress in Nuclear Energy*, 134, 103674.

Elloumi, H., M. Stambouli, J. J. Damelincourt, and B. Mrabet, 2002: Integrating Cylinder Radiometry and Photometry: Application to Radiant Flux and Irradiance Measurements. *Journal of Quantitative Spectroscopy and Radiative Transfer,* 74, 731–44.
(Elloumi et al., 2002)

Hidy, G. M., 2019: Atmospheric Chemistry in a Box or a Bag. *Atmosphere*, 10, 401. (Hidy, 2019)

Huang, Q. T. Liu, J. Yang, L. Yao, and L. Gao, 2011: Evaluation of Radiative Transfer Using the Finite Volume Method in Cylindrical Photoreactors. *Chemical Engineering Science* 66, 3930–3940. (Huang et al., 2011)

Hulstrom, R., R. Bird, and C. Riordan, 1985: Spectral Solar Irradiance Data Sets for Selected Terrestrial Conditions. *Solar Cells,* 15, 365–91. (Hulstrom et al., 1985)

Insight, Ocean. 2018. "Flame Miniature Spectrometer User Manual." Ocean User Manuals. https://www.manualslib.com/manual/1439052/Ocean-Optics-Flame-S.html

Kasap, S., and P. Capper (eds.), 2017: *Springer Handbook of Electronic and Photonic Materials*, 2nd ed., Springer, 1536pp. (Kasap and Capper, 2017)

Koo, Y. H., Y. S. Yang, and K. W. Song, 2014: Radioactivity Release from the Fukushima Accident and Its Consequences: A Review. *Progress in Nuclear Energy*, 74, 61–70. (Koo et al. 2014)

Michael, P. 2019. "A Conversion Guide: Solar Irradiance and Lux Illuminance." *IEEE Datasets*. doi: https://dx.doi.org/10.21227/mxr7-p365.

Ocean Insight, 2019. "Why Collimating Lenses Are So Important Use Collimators to Align Light in Your Spectrometer Setup." Ocean News Releases, 4–7.
https://www.oceaninsight.com/products/sampling-accessories/free-space-optics/collimating-lenses/collimating-lenses/

Osram. 2016. "XBO® Theater Lamps." https://www.osram.com/ecat/XBO%20Xenon%20short-arc%20lamps%20without%20reflector-XBO%20Xenon%20short-arc%20lamps-Discharge%20lamps-Industry-Specialty%20Lighting/com/en/GPS01_1028545/

Ostroumova, E., A. Rozhko, M. Hatch, K. Furukawa, O. Polyanskaya, R. J. McConnell, E. Nadyrov, S. Petrenko, G. Romanov, V. Yauseyenka, V. Drozdovitch, V. Minenko, A. Prokopovich, I. Savasteeva, L. B. Zablotska, K. Mabuchi, and A. V. Brenner, 2013: Measures of Thyroid Function among Belarusian Children and Adolescents Exposed to Iodine-131 from the Accident at the Chernobyl Nuclear Plant. *Environmental Health Perspectives*, 121, 865–71. (Ostroumova et al., 2013)

Pareek, V., S. Chong, M. Tade, A. A. Adesina, 2008: Light intensity distribution in heterogenous photocatalytic reactors. *Asia-Pacific Journal of Chemical Engineering*, 3, 171-201. (Pareek et al. 2008)

Romero, R. L., O. M. Alfano, and A. E. Cassano, 1997: "Cylindrical Photocatalytic Reactors. Radiation Absorption and Scattering Effects Produced by Suspended Fine Particles in an Annular Space." *Industrial and Engineering Chemistry Research*, 36, 3094–3109. (Romero et al., 1997)

Saiz-Lopez, A., J. M. C. Plane, A. R. Baker, L. J. Carpenter, R. Von Glasow, J. C. Gómez Martín, G. McFiggans, and R.W. Saunders, 2012: Atmospheric Chemistry of Iodine. *Chemical Reviews*, 112, 1773–1804. (Saiz-Lopez et al. 2012)

Sommariva, R., W. J. Bloss, and R. Von Glasow, 2012: Uncertainties in Gas-Phase Atmospheric Iodine Chemistry. *Atmospheric Environment*, 57, 219–32. (Sommariva et al. 2012)

7.0 Acknowledgements

Pacific Northwest National Laboratory

902 Battelle Boulevard
P.O. Box 999
Richland, WA 99354
1-888-375-PNNL (7665)

www.pnnl.gov